Proposal for implementing Stiefel-Whitney insulators in an optical Raman lattice

Jian-Te Wang,[1,2] Jing-Xin Liu,[1,2] Hai-Tao Ding,[1,2] and Peng He[3,*]

[1]*National Laboratory of Solid State Microstructures, School of Physics, and Collaborative Innovation Center of Advanced Microstructures, Nanjing University, Nanjing 210093, China*

[2]*Key Laboratory of Atomic and Subatomic Structure and Quantum Control (Ministry of Education), Guangdong Basic Research Center of Excellence for Structure and Fundamental Interactions of Matter, School of Physics, South China Normal University, Guangzhou 510006, China*

[3]*Department of Physics, Guangdong-Hong Kong Joint Laboratory of Quantum Matter, The University of Hong Kong, Pokfulam Road, Hong Kong, China*

(Received 5 February 2024; accepted 6 May 2024; published 21 May 2024)

The Stiefel-Whitney insultor is a two-dimensional topological insulator protected by parity-time ($\mathcal{PT}$) symmetry. With a vanishing Chern number, the topology in this system is characterized by second Stiefel-Whitney class. We propose a feasible scheme to realize a four-band Stiefel-Whitney insultor with spin-orbit coupled ultracold atoms in an optical Raman lattice. Four selected spin states are coupled by carefully designed Raman lasers to generate the desired spin-orbit interactions with spacetime inversion symmetry. We map out a phase diagram with respect to the experimental parameters, where a large topological phase region exists. We further present two distinct detection methods to resolve the non-Abelian band topology, in both equilibrium and dynamical ways. The detection relies on the spin textures extracted from the time-of-flight imaging, showing the tomographic signatures in the ground states and long-time averaged patterns on certain submanifolds via a bulk-surface duality. Our work paves a realistic way to explore novel topology inside real Berry bundles with quantum matters.

DOI: 10.1103/PhysRevA.109.053314

I. INTRODUCTION

The study of topological insulators (TIs) has been a major focus in ultracold atoms [1–4] and condensed matter physics [5–8] in recent decades. The early tenfold classification based on fundamental symmetries, including antiunitary time-reversal $\mathcal{T}$, particle-hole $\mathcal{C}$, and chiral $\mathcal{S}$ symmetry in noninteracting fermionic systems, highlights the central role of the system symmetries [9–11]. This approach has been extended to unitary spatial symmetries [12,13], leading to the theoretical discovery of crystalline-symmetry-protected topological phases, such as the fragile topological insulators [14–18] and the higher-order topological insulators [19–22]. In particular, the topological Euler phase and Stiefel-Whitney insulator (SWI) protected by the combined symmetry of $\mathcal{PT}$ with spatial inversion ($\mathcal{P}$) or the two-fold rotations and TRS ($\mathcal{C}_2\mathcal{T}$) has attracted considerable interest [23–32]. The SWI is characterized by the second Stiefel-Whitney (SW) class of the real ground states imposed by the protecting symmetry, which is a crystalline-protected analog of the Chern number. The classification based on orthogonal K-theory for the single-gap topology has been established [33], and the non-Abelian aspect of multigap topology has been widely explored [26,30]. Meanwhile, the SWI also manifests its intriguing features in the semimetallic phases, such as the existence of the point nodes and line nodes carrying a $\mathbb{Z}_2$ monopole charge [23,24,28], and higher dimensional generalizations [34,35]. Therefore, it is of paramount importance to verify the theoretical findings in a feasible experimental setup.

Ultracold atoms [1,2] provide a versatile platform for quantum simulation due to the high tunability of the atom-light interactions [36–45]. The creation of artificial gauge fields [46–53] and spin-orbit coupling (SOC) [54–64] has led to a plethora of experimental demonstrations of topological phases [65–70]. The fast development of detection approaches based on dynamical response [71–77] and band tomography [78–83] has also contributed greatly to experimental progress. However, previous experiments usually involve only Abelian bands in an optical lattice. The engineering and detection of topological bands with degeneracy and stabilized by certain symmetries are still challenging.

In this paper we propose a practical approach to realizing a two-dimensional (2D) $\mathcal{PT}$-symmetric SWI in an optical Raman lattice. We include four selected spin states in the ground-state manifold so that transitions driven by the same Raman potentials share identical Clebsch-Gordan coefficients. This results in the desired real hopping events, which give rise to a low-energy s-band model that naturally preserves the $\mathcal{PT}$ symmetry. The two degenerate s bands are indexed by the second SW class. We map out a phase diagram according to the second SW class and find a robust region of SWI on the phase plane. Since the total Chern number is zero and the degeneracy for occupied bands in SWI doesn't possess any featured points in momentum space, detection through Hall drift [74,75] and Ramsey interferometry [71–73]

*penghe@hku.hk

is not suitable. To overcome this obstacle, we further show the robustness of the SWI in our model by introducing a $\mathcal{T}$-broken term modified under an external magnetic field. We also provide two detection methods to resolve the non-Abelian band topology, based on equilibrium and dynamical schemes. The equilibrium scheme requires tomography of the prepared degenerate ground state through the quasimomentum distribution of the spin textures extracted from time-of-flight (TOF) imaging. To circumvent the O(2) gauge mixing of the raw data from state tomography, we apply a parallel transport gauge and calculate the second SW class, giving a direct probe of the topology. The dynamical scheme probes the unitary evolution following a sudden quench. The topological information is rebuilt by the long-time averaged spin textures on the reduced quasimomentum submanifold called the band inversion surface (BIS), which is defined by the quenching axis. We show the bulk-surface duality for our model by generalizing the original $\mathbb{Z}$ class case [84–86].

The rest of this paper is organized as follows. In Sec. II we introduce the concept and formulation of our target SWI model and second SW class. In Sec. III we present a Raman scheme coupling four selected internal states for alkali atoms to realize a 2D SWI in a square optical lattice. To reveal nontrivial topology in our proposed model, two distinct detection methods are discussed, with an equilibrium scheme shown in Sec. IV and a dynamical one shown in Sec. V, based on achievable experimental techniques.

II. SW INSULATOR

Under a preserved spinless parity-time $\mathcal{PT} = \mathcal{K}$ symmetry, the SWI stands for a two-dimensional topological insulating phase characterized by a $\mathbb{Z}_2$ index called second SW class. Such a Bloch Hamiltonian must obey $(\mathcal{PT})\mathcal{H}(\boldsymbol{k})(\mathcal{PT})^{-1} = \mathcal{H}(\boldsymbol{k})$ and thus has a representation containing only real elements, along with a set of real eigenstates. In particular, we choose the set of real Dirac matrices satisfying the Clifford algebra as $\gamma_1 = \sigma_1 \otimes \tau_0$, $\gamma_2 = \sigma_2 \otimes \tau_2$, $\gamma_3 = \sigma_3 \otimes \tau_0$, while the other two Dirac matrices $\gamma_4 = \sigma_2 \otimes \tau_1$ and $\gamma_5 = \sigma_2 \otimes \tau_3$ are purely imaginary, with σ_i and τ_i being two sets of the Pauli matrices and σ_0 and τ_0 being the 2×2 identity matrix. A four-band Bloch SWI Hamiltonian can be constructed in a compact form [33]:

$$\mathcal{H}(\boldsymbol{k}) = \boldsymbol{d} \cdot \boldsymbol{\gamma} + m_z \tau_3, \tag{1}$$

where $d_1 = 2t_1 \sin k_y$, $d_2 = 2t_2 \sin k_x$, $d_3 = \delta_V - 2t_3(\cos k_x + \cos k_y)$. The energy of four Bloch bands are $\varepsilon_{n,\pm}(\boldsymbol{k}) = (-1)^{(n)}\sqrt{(\sqrt{d_1^2 + d_3^2} \pm m_z)^2 + d_2^2}$ $(n = 1, 2)$, in which two valence bands with $n = 1$ are globally degenerate for $m_z = 0$, otherwise they have only two accidental degeneracy points residing at $\boldsymbol{K}_\pm = (\pm \cos^{-1}[\delta_V/(2t_3) - 1], 0)$ or $(\pm \cos^{-1}[\delta_V/(2t_3) + 1], \pi)$.

For two occupied bands, the second SW class can be calculated by [24,26]

$$\nu = \frac{1}{4\pi} \int_{T^2} \mathrm{Tr}[I\mathcal{F}_R]\, dk_x\, dk_y \mod 2,$$
$$\equiv \frac{1}{2\pi} \int_{T^2} \mathcal{F}_R^{12}\, dk_x\, dk_y \mod 2, \tag{2}$$

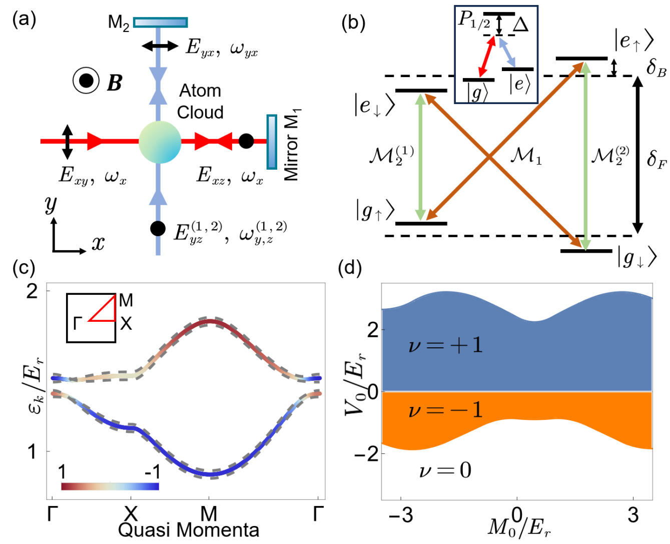

FIG. 1. (a) Schematic of the setup for realizing the Stiefel-Whitney insulator (SWI). The cold atom cloud is confined by a magnetic trap and illuminated by laser fields, $\boldsymbol{E}_x$ and $\boldsymbol{E}_y$, reflected by mirrors, which create 2D optical lattice potentials and Raman couplings in the x-y plane. (b) Related Raman transitions between the involved spin states. Raman transitions $\mathcal{M}_1^{(1,2)}$ and $\mathcal{M}_2$ are driven by distinctive two-photon processes with individual polarization and frequency configurations. All these two-photon processes occur between $|e\rangle$ and $|g\rangle$ states, as shown in the inset. (c) The s-band structures along the high-symmetry lines in the first Brillouin zone (shown in the inset) for the $\mathcal{T}^2 = -1$ symmetric case (solid lines, $m_z = 0$) and the broken case (dashed lines, $m_z = 0.065E_r$). The color indicates the value of $\langle\gamma_3\rangle$ for the corresponding eigenstates. The global degeneracy is lifted in the broken case. Parameters are chosen as $V_0 = 3E_r$, $M_{10} = M_{20} = M_0 = E_r$, and $\delta_V = 0.3V_0$. (d) The second SW class of the lowest bands with respect to the lattice depth V_0 and the Raman coupling strength M_0. $E_r = (\hbar k_L)/2m_a$ is the recoil energy, with m_a being the mass of the atom.

where $I = -i\sigma_2$ is the generator of the SO(2) group, and $\mathcal{F}_R = [\nabla_{\boldsymbol{k}} \times \boldsymbol{A}(\boldsymbol{k})]_z$ is the skew-symmetric non-Abelian Berry curvature for the real bundle with the real Berry connection $\boldsymbol{A}^{mn}(\boldsymbol{k}) = \langle u_{\boldsymbol{k}}^m | \nabla_{\boldsymbol{k}} | u_{\boldsymbol{k}}^n \rangle$, and $|u_{\boldsymbol{k}}^n\rangle$ is a real occupied Bloch state. Remarkably, the $\mathbb{Z}_2$ nature arises from the reduced orthogonal K group, $\widetilde{KO}(S^2) \cong \mathbb{Z}_2$ [24] and indicates the existence of topological obstruction for representing the real occupied states in spin structure. As shown in Eq. (1), besides $\mathcal{PT} = \mathcal{K}$ symmetry, the proposed Hamiltonian also respects the single $\mathcal{P}$ and $\mathcal{T}^2 = 1$ symmetry, with $\mathcal{P} = \gamma_3$ and $\mathcal{T} = \gamma_3\mathcal{K}$, and additional $\mathcal{T}^2 = -1$ symmetry only when $m_z = 0$. For more discussion on extra symmetries, see Appendix A. The perturbation $m_z\tau_3$ distinguishes the SWI phase from $\mathcal{T}$-invariant TIs in two dimensions.

III. MODEL REALIZATION

In this section we propose a possible experimental scheme to realize the SWI model (1) with ultracold alkali atoms in an 2D tunable optical Raman lattice, as illustrated in Figs. 1(a) and 1(b). To implement the real Bloch bands, we use four Zeeman-split ground hyperfine levels in ground-state manifold $S_{1/2}$, namely, $|e_{\uparrow,\downarrow}\rangle = |F+1, m_F = 1, -1\rangle$ and

$|g_{\uparrow,\downarrow}\rangle = |F, m_F = -1, 1\rangle$, with the energy landscape shown in Fig. 1(b), in which the Zeeman shift is $\delta_B(-\delta_B)$ for $|\uparrow(\downarrow)\rangle$ subspace. The lattice and Raman potentials are both generated by standing-wave light fields given by a monochrome $\boldsymbol{E}_x$ and a multifrequency $\boldsymbol{E}_y$, namely, $\boldsymbol{E}_x = E_{xz}\boldsymbol{e}_z \cos k_L x + \mathrm{i}E_{xy}\boldsymbol{e}_y \sin k_L x$, and $\boldsymbol{E}_y = \sum_{i=1,2} E_{yz}^{(i)}\boldsymbol{e}_z \sin k_L y + E_{yx}\boldsymbol{e}_x \cos k_L y$, where $E_{\mu\nu}(\mu, \nu = x, y, z)$ are field components propagating in the direction μ with polarization ν, the wave number k_L of $\boldsymbol{E}_x$ and $\boldsymbol{E}_y$ is approximately the same, and all other irrelevant phases in light fields are ignored. The frequency difference between the two sets of beams compensates the Zeeman splitting as $\omega_{xy} - \omega_{yx} = \delta_F$, $\omega_{xz} - \omega_{yz}^{(1)} = \delta_F - 2\delta_B$, and $\omega_{xz} - \omega_{yz}^{(2)} = \delta_F + 2\delta_B$, in which δ_F is the initial hyperfine splitting between $|F\rangle$ and $|F+1\rangle$ (about several GHz). Affected by these light fields, we show below that the motion of atoms is governed by the following Hamiltonian (more details can be found in Appendix B):

$$H = \left[\frac{\boldsymbol{p}^2}{2m_a} \otimes \mathbf{1} + \hat{V}_{\text{latt}}(\boldsymbol{r})\right] + \mathcal{M}_1(\boldsymbol{r})\gamma_1 + \mathcal{M}_2(\boldsymbol{r})\gamma_2 + m_z\tau_3, \tag{3}$$

where m_a is the atomic mass and m_z is obtained by slightly tuning Zeeman field strength.

The lattice potential $\hat{V}_{\text{latt}} \propto (\boldsymbol{E}_x^* \cdot \boldsymbol{E}_x + \boldsymbol{E}_y^* \cdot \boldsymbol{E}_y)$ is generally anisotropic in the x-y plane and forms a spin-dependent square lattice, taking the form $\hat{V}_{\text{latt}}(x, y) = (V_x \otimes \mathbf{1} + \delta V_x\gamma_3)\cos^2(k_L x) + (V_y \otimes \mathbf{1} + \delta V_y\gamma_3)\cos^2(k_L y)$, in which a constant term is dropped. Without loss of generality, we consider the isotropic case and take $V_x = V_y = V_0$, and $\delta V_x = \delta V_y = \delta_V$ thereafter.

The Raman potential $\mathcal{M}_1(\boldsymbol{r})$ and $\mathcal{M}_2(\boldsymbol{r})$ are generated by two-photon processes between $\boldsymbol{E}_x$ and $\boldsymbol{E}_y$. Due to the selection rule, one Raman potential $\mathcal{M}_1(\boldsymbol{r}) = M_{10}\sin(k_L x)\cos(k_L y)$ with $M_{10} \propto (\frac{1}{\Delta_1} - \frac{1}{\Delta_2})E_{xy}E_{yx}$ can be generated only by E_{xy} and E_{yx} components. The other is driven by two distinctive processes contributed from E_{xz} and $E_{yz}^{(1,2)}$, with $\mathcal{M}_2(\boldsymbol{r}) = M_{20}\sin(k_L y)\cos(k_L x)$ in which $M_{20} \propto (\frac{1}{\Delta_1} - \frac{1}{\Delta_2})E_{xz}E_{yz}$, where we just set $E_{yz} \equiv E_{yz}^{(1)} = E_{yz}^{(2)}$.

The key ideas of generating required Raman potential are summarized as follows. First, the choice of spin states is symmetric relative to $m_F = 0$, which guarantees the strength between two simultaneously driven parts in γ_1 term is equal. Moreover, the bias Zeeman field forbids possible contribution from E_{xy} and E_{yx} in the γ_2 term by lifting degeneracy. These features ensure the validity of our proposal.

We further take that bosons occupy the lowest s orbitals $\phi_{s,\sigma\tau}$ $(\sigma = e, g,\ \tau = \uparrow, \downarrow)$, and consider only the nearest-neighbor hoppings. Then we derive a tight-binding Hamiltonian,

$$\begin{aligned} H_s = &\sum_{\langle\mathbf{ij}\rangle,\sigma\neq\sigma',\tau} t_1^{\mathbf{ij}} c_{\mathbf{i},\sigma,\tau}^{\dagger} c_{\mathbf{j},\sigma',\tau} + \sum_{\langle\mathbf{ij}\rangle,\sigma\neq\sigma'} t_2^{\mathbf{ij}} (c_{\mathbf{i},\sigma,\uparrow}^{\dagger} c_{\mathbf{j},\sigma',\downarrow} \\ &- c_{\mathbf{i},\sigma,\downarrow}^{\dagger} c_{\mathbf{j},\sigma',\uparrow}) + \sum_{\langle\mathbf{ij}\rangle,\sigma,\tau} t_{\sigma}^{\mathbf{ij}} c_{\mathbf{i},\sigma,\tau}^{\dagger} c_{\mathbf{j},\sigma,\tau} \\ &+ \sum_{\mathbf{i}} m_z(n_{\mathbf{i},\uparrow} - n_{\mathbf{i},\downarrow}) + \delta_V(n_{\mathbf{i},e} - n_{\mathbf{i},g}), \end{aligned} \tag{4}$$

where $c_{\mathbf{i},\sigma,\tau}^{\dagger}$ $(c_{\mathbf{i},\sigma,\tau})$ is the creation (annihilation) operator with $\mathbf{i} = (i_x, i_y)$ denoting the lattice sites, the notation $\langle\mathbf{ij}\rangle$ runs over all nearest-neighbor sites, and $n_{\mathbf{i},\sigma(\tau)} = \sum_{\tau(\sigma)} c_{\mathbf{i},\sigma,\tau}^{\dagger} c_{\mathbf{i},\sigma,\tau}$ is the particle number operator. The strengths of related spin-flipped nearest-neighbor hoppings are given by

$$\begin{aligned} t_1^{\vec{i}\vec{j}} &= \int d^2\boldsymbol{r}\phi_{s,e\uparrow}^{(i)}[M_{10}\sin(k_L x)\cos(k_L y)]\phi_{s,g\uparrow}^{(j)}, \\ t_2^{\vec{i}\vec{j}} &= \int d^2\boldsymbol{r}\phi_{s,e\uparrow}^{(i)}[M_{20}\sin(k_L y)\cos(k_L x)]\phi_{s,g\downarrow}^{(j)}, \end{aligned} \tag{5}$$

while the strengths of spin-conserved hoppings are given by

$$\begin{aligned} t_e^{\vec{i}\vec{j}} &= \int d^2\boldsymbol{r}\phi_{s,e\sigma}^{(i)}\left[\frac{\boldsymbol{p}^2}{2m_a} + V_+(\cos^2 k_L x + \cos^2 k_L y)\right]\phi_{s,e\sigma}^{(j)}, \\ t_g^{\vec{i}\vec{j}} &= \int d^2\boldsymbol{r}\phi_{s,g\sigma}^{(i)}\left[\frac{\boldsymbol{p}^2}{2m_a} + V_-(\cos^2 k_L x + \cos^2 k_L y)\right]\phi_{s,g\sigma}^{(j)}, \end{aligned} \tag{6}$$

with $V_\pm = V_0 \pm \delta_V$. We further perform a gauge transformation $c_{\mathbf{i},g,\tau} \to e^{-i\pi(i_x+i_y)}c_{\mathbf{i},g,\tau}$ to absorb the staggered sign in the spin-flipped hopping terms. After Fourier transformation, the Bloch Hamiltonian in $\boldsymbol{k}$ space reads $H_{s,\boldsymbol{k}} = \sum_{\boldsymbol{k}} c_{\boldsymbol{k}}^{\dagger}\mathcal{H}(\boldsymbol{k})c_{\boldsymbol{k}}$, with $c_{\boldsymbol{k}} = (c_{\boldsymbol{k},e\uparrow}, c_{\boldsymbol{k},e\downarrow}, c_{\boldsymbol{k},g\uparrow}, c_{\boldsymbol{k},g\downarrow})^{\mathrm{T}}$, equal to Eq. (1) except for additional term $2t_0(\cos k_x + \cos k_y)\gamma_0$, where γ_0 is 4×4 identity matrix and has no physical significance.

We numerically solve the continuous Hamiltonian (3) using a Fourier series expansion of a Bloch function (see Appendix C). The structure of the lowest s bands is shown in Fig. 1(c). The inversion of the spin polarization $\langle\gamma_3\rangle$ in the valence and conduction bands reveals the band repulsion induced by the SOC, indicating the topological nature of our model. This inspires a method to detect the topology of our model, as we will discuss later. Furthermore, we map out the phase diagram of the continuous Hamiltonian (3) based on the second SW class of the valence bands. The second SW class is numerically calculated using the four parities of the Bloch states at high symmetric momentum points. We find a large nontrivial regime on the phase plane in Fig. 1(d), which is accessible with current technology. Two regimes with $\nu = \pm 1$ are topologically equivalent due to their $\mathbb{Z}_2$ nature, but they are separated by a gap-closing event where $V_0 = \delta_V = 0$.

IV. EQUILIBRIUM DETECTION

We now proceed to the direct probe of the second SW class via an O(2) link method. We assume that the system is prepared in its ground state with a half-filling condition,

$$|G\rangle = \prod_{\mathbf{k}} a_{\mathbf{k},1+}^{\dagger} \prod_{\mathbf{k}} a_{\mathbf{k},1-}^{\dagger}|0\rangle, \tag{7}$$

where $a_{\mathbf{k},1\pm}^{\dagger}$ are occupied eigenmodes, related to Bloch states expressed in the spin basis by $|u_{\mathbf{k}}^{\alpha}\rangle = a_{\mathbf{k},\alpha}^{\dagger}|0\rangle = \sum_{\beta}[u_{\mathbf{k}}^{\alpha}]^{\beta}c_{\mathbf{k},\beta}^{\dagger}|0\rangle$, in which $[u_{\mathbf{k}}^{\alpha}]^{\beta}$ is the β component with a real value.

With the system cooling down to the ground state, we then turn off the optical potential and perform TOF imaging from which we obtain quasimomentum distribution of occupied states $n_{\beta}(\mathbf{k}) = \sum_{\pm}|[u_{\mathbf{k}}^{1\pm}]^{\beta}|^2$ with contributions of the two degenerate bands. Following [82,83], we're able to separately extract the Bloch states through an impulsive pulse

TABLE I. Numerical results for topological index ν in different realistic conditions (with periodic or open boundaries, with or without trap). The size of the lattice is uniformly set to be 8×8. The depth of harmonic trap is given by $\mu_T/t_1 = 0.01$. Other parameters are $t_2/t_1 = t_3/t_1 = 1$, $m_z/t_1 = 0.4$.

δ_V/t_1	Periodic	Open	Periodic+Trap	Open+Trap
2	1.000	1.000	1.000	0.999
8	0	0	0	0

right before TOF to induce a rotation between different spin components, which generally transform expectation values of arbitrary Hermitian unitary matrices into measurable occupations. Notice that rotations combining $|e\rangle$ and $|g\rangle$ ought to be realized through Raman processes rather than conventional radiofrequency or microwave pulses since those states carry different momenta [83]. These Raman pulses can be applied through incident resonant Raman processes with tunable relative and total phases. By canceling retroreflective beams in Fig. 1(a), lattice potentials vanish. The remaining Raman fields generated by traveling light fields can effectively bring spinful rotations. For instance, we choose rotations as $T_1 = e^{i\frac{\pi}{4}\sigma_2}$ and $T_2 = e^{i\frac{\pi}{4}\gamma_4}$, in which T_1 transforms Bloch components $[u_{\mathbf{k}}^{1\pm}]^1$ to $\frac{1}{\sqrt{2}}([u_{\mathbf{k}}^{1\pm}]^1 + [u_{\mathbf{k}}^{1\pm}]^3)$, and T_2 transforms $[u_{\mathbf{k}}^{1\pm}]^1$ to $\frac{1}{\sqrt{2}}([u_{\mathbf{k}}^{1\pm}]^1 + [u_{\mathbf{k}}^{1\pm}]^4)$. In this way, we obtain the full tomography of the Bloch states in $\mathcal{H}(\mathbf{k})$ when $m_z = 0$ (see Appendix D for details). Then we discretize the TOF image and define a connection matrix of Bloch states at the near-quasimomentum pixel, $[\theta_{\mathbf{k}}^{x(y)}]$ by $[\theta_{\mathbf{k}}^{x(y)}]^{\alpha\beta} = \langle u^{\alpha}_{\mathbf{k}+\delta\mathbf{k_x}(\mathbf{k_y})} | u^{\beta}_{\mathbf{k}} \rangle$, in the spirit of a real Wilson loop. An O(2) link is given by

$$\mathcal{W}_{\mathbf{k}} = [\theta_{\mathbf{k}}^{y}]^{-1}[\theta_{\mathbf{k}+\delta\mathbf{y}}^{x}]^{-1}[\theta_{\mathbf{k}+\delta\mathbf{x}}^{y}][\theta_{\mathbf{k}}^{x}]. \quad (8)$$

$[\theta_{\mathbf{k}}^{x(y)}]$ at each quasimomentum $\mathbf{k}$ corresponds to an SO(2) Berry rotation with $\det[\theta] = +1$ or -1, due to the discontinuity of the O(2) group. Therefore, in the most general case, $\mathcal{W}_{\mathbf{k}}$ is gauge-covariant. Under a local gauge transformation $\mathcal{O}_{\mathbf{k}}^{-1}\mathcal{W}_{\mathbf{k}}\mathcal{O}(\mathbf{k})$ with $\det[\mathcal{O}] = -1$, the sign of $\mathcal{W}_{\mathbf{k}}$ changes. Therefore, we need to apply a parallel transport gauge to fix the orientation of the O(2) link [87]. After doing this, we build a gauge-independent field by $\mathcal{F}_{xy} = i \ln \mathcal{W} = i\theta_{\mathbf{k}}^{\text{tot}}\sigma_2$, corresponding to a discrete version of the non-Abelian real Berry curvature. The Euler class is then calculated by summing them up in the Brillouin zone: $\nu = \frac{1}{2\pi}\sum_{\mathbf{k}} \theta_{\mathbf{k}}^{\text{tot}}$.

To verify our method, we simulate the experimental signals by diagonalizing the real-space Hamiltonian on a finite lattice and using Fourier transformation [88,89], as shown in Fig. 2. To simulate realistic experiments, we add a global harmonic trap $V_{\text{trap}} = \frac{1}{2}m_a\omega^2 r^2$, which is parameterized by $\frac{\mu_T}{t_1} = \frac{1}{2}m_a\omega^2 a^2$. We also compare the results under different boundary conditions in Appendix D and summarize them in Table I, which agree well with each other. Numerical calculations show that our method works well even for lattices with very small sites and near the phase boundary.

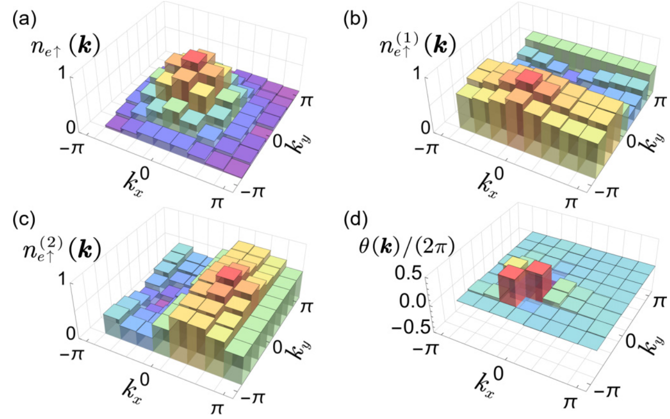

FIG. 2. Density distributions of the spin states for $n_{e\uparrow}$ with (a) no pulses added, (b) added T_1, and (c) added T_2 in momentum space for a finite periodic lattice with 8×8 sites. The total density at each point is $\sum_i n_i(\boldsymbol{k}) = 2$, corresponding to a half-filling case. (d) Extracted real Berry curvature at discretized Brillouin zone. The summation gives the second SW class $\nu = 1$. Parameters are chosen as $t_2/t_1 = t_3/t_1 = 1$, $\delta_V/t_1 = 2$, and $m_z = 0$.

V. DYNAMICAL DETECTION

The equilibrium detection requires the preparation of a nontrivial ground state. Next, we propose to probe the topology by quench dynamics [27,79] (applied to the case where $m_z = 0$) that starts from a trivial initial state, and detect the time-averaged outcome within certain submanifolds inside the Brillouin zone. The system is initialized in the deeply trivial regime, then quenched to a target post-Hamiltonian. The initial state is thus fully polarized in the ground state of a prequench Hamiltonian $H_0 = m_i\gamma_i$ with a very large mass term parallel to a fixed quench axis (the choice of axis can be arbitrary, but we specifically choose γ_2 to illustrate our method). The time-averaged spin polarization (TASP) $\langle\overline{\gamma_i}\rangle$ at $\boldsymbol{k}$ is given by

$$\begin{aligned}\langle\overline{\gamma_i}\rangle(\boldsymbol{k}) &= \frac{1}{T}\int_0^T \langle\Psi^0|c_{\boldsymbol{k}}^{\dagger}[e^{iH_{\boldsymbol{k}}^t t}\gamma_i e^{-iH_{\boldsymbol{k}}^t t}]c_{\boldsymbol{k}}|\Psi^0\rangle \\ &= -d_i(\boldsymbol{k})d_2(\boldsymbol{k})/[\varepsilon(\boldsymbol{k}) - d_0(\boldsymbol{k})]^2, \end{aligned} \quad (9)$$

where $H_{\mathbf{k}}^t = \boldsymbol{d}(\mathbf{k}) \cdot \boldsymbol{\gamma}$ is the postquench Hamiltonian, and T is the evolution time after the quench. We plot the numerical results in Fig. 3. The TASP $\gamma \equiv (\langle\overline{\gamma_1}\rangle, \langle\overline{\gamma_3}\rangle)$ vanishes on a reduced structure called the BIS ($\mathcal{B}_1$), defined by $\mathcal{B}_1 = \{\mathbf{k}|d_2(\mathbf{k}) = 0\}$. For the case with γ_2 as the quench axis, $\mathcal{B}_1$ is simply $k_x = 0, \pi$. Furthermore, a certain component $\langle\overline{\gamma_i}\rangle$ of the TASP also vanishes on $\mathcal{B}_1' = \{\mathbf{k}|d_i(\mathbf{k}) = 0\}$, and its intersection with $\mathcal{B}_1$ gives rise to a higher-order BIS ($\mathcal{B}_2$) defined by $\mathcal{B}_2 = \{\mathbf{k}|d_2 = d_i = 0\}$. As shown in Fig. 3(b), the spin vector γ exhibits nontrivial winding behavior across $\mathcal{B}_1$ in the topological case. This feature is captured by a field $\mathbf{g}(\mathbf{k}) = \frac{1}{\mathcal{N}_{\mathbf{k}}}\partial_{\mathbf{k}_\perp}\gamma$, where $\mathbf{k}_\perp$ denotes the momentum perpendicular to $\mathcal{B}_1$, and $1/\mathcal{N}_{\mathbf{k}}$ is the normalization factor. We show that the winding number of the field $\mathbf{g}(\mathbf{k})$ on the submanifold $\mathcal{B}_1$, $w_1 = \sum_i \int_{\mathcal{B}_1^{(i)}} \mathrm{d}\mathbf{k}\, \mathbf{g}(\mathbf{k}) \cdot \mathrm{d}\mathbf{g}(\mathbf{k})$, is equivalent to the second Stiefel-Whitney class (for a brief proof, see Appendix E). We can understand this connection through the gauge transition between the two patches divided by the BIS [33]. This

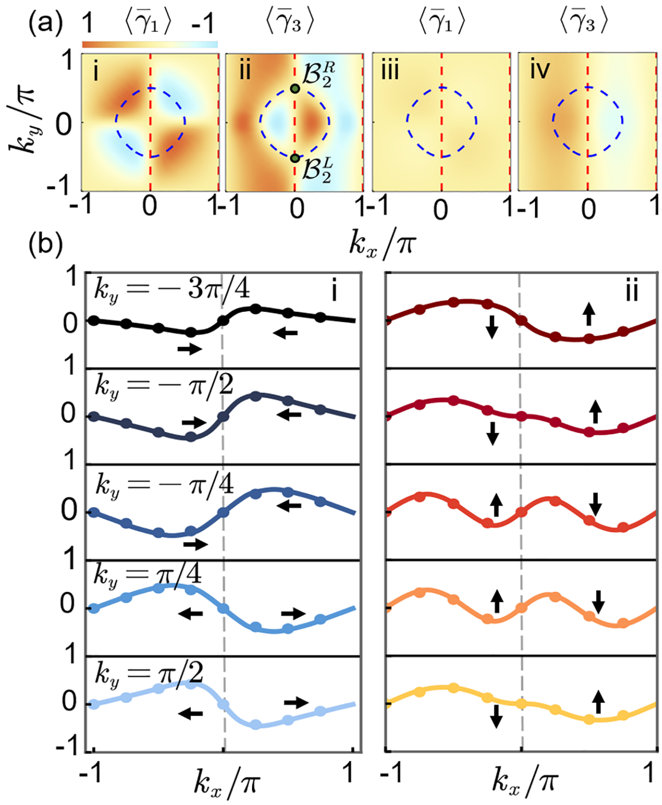

FIG. 3. (a) Time-averaged spin polarization calculated using the Bloch Hamiltonian for (i) $\langle\overline{\gamma_1}\rangle$ and (ii) $\langle\overline{\gamma_3}\rangle$ in the topological phase ($\delta_V = 1$) and (iii) $\langle\overline{\gamma_1}\rangle$ and (iv) $\langle\overline{\gamma_3}\rangle$ in the trivial phase ($\delta_V = 4$). The quench axis is γ_2, with a ring-shaped BIS defined by $d_3(\boldsymbol{k}) = 0$, and a line-shaped BIS defined by $d_2(\boldsymbol{k}) = 0$. (b) The sector of the TASP in the topological phase calculated using the Bloch Hamiltonian (lines) and finite real space lattice (solid circles). The arrows show the rotation directions of the spin vector $\boldsymbol{\gamma} = (\langle\overline{\gamma_1}\rangle, \langle\overline{\gamma_3}\rangle)$ across the BIS (along the $+k_x$ direction). For the finite system, the size is 8×8 with an extra harmonic trap with $\mu_T/t_1 = 0.01$. The evolution time after quenching is $T/t_1 = 20$. Here we take $\hbar = 1$.

correspondence builds a non-Abelian version of the dynamical bulk-surface duality for our system. The detection can even be further reduced to the second-order BIS ($\mathcal{B}_2$). The topology then relies on the parity of $\mathcal{B}_2$, $\nu = \frac{1}{2}\sum_{\mathcal{B}_2} \mathrm{sgn}(d_{3,L}) - \mathrm{sgn}(d_{3,R})$.

VI. CONCLUSIONS

In summary, we have proposed a feasible scheme to realize a four-band $\mathcal{PT}$-symmetric SWI in an optical Raman lattice, along with two different methods to detect nontrivial topology in our model. The proposed realization is discussed based on a natural Raman lattice approach, which is suitable for all alkali atoms with half-integer nuclear spins. Further detection methods are given for both the equilibrium and nonequilibrium cases. Through mathematical derivation and numerical simulation, we show the equivalence of some variations of the topological index in SWI and address the validity of these methods under realistic experimental imperfections, such as limited system size, different boundary conditions, and the existence of an extra harmonic potential. Furthermore, these detection methods are not limited by $\mathbb{Z}_2$ classification and can be directly applied to topological Euler phases. Our proposed system would provide a promising platform for elucidating the exotic physics of SWI that is elusive in nature and may be realized with various artificial quantum systems [1,2,90–95].

ACKNOWLEDGMENTS

We thank Y. Q. Zhu, Zhen Zheng, and S. L. Zhu for helpful discussions. This work was supported by the National Natural Science Foundation of China (Grant No. 12074180).

APPENDIX A: SYMMETRIES IN REALIZED MODEL

In this Appendix we discuss extra symmetries in the proposed $(\mathcal{PT})^2 = 1$ symmetric model. We recall the form of the Bloch Hamiltonian,

$$\mathcal{H}_{\boldsymbol{k}} = m_z\tau_3 + 2t_1 \sin k_y\gamma_1 + 2t_2 \sin k_x\gamma_2 + [\delta_V - 2t_3(\cos k_x + \cos k_y)]\gamma_3, \tag{A1}$$

with $2t_0(\cos k_x + \cos k_y)$ as a uniform hopping term. In all chosen sets of parameters, Eq. (A1) preserves $(\mathcal{PT})\mathcal{H}_{\boldsymbol{k}}(\mathcal{PT})^{-1} = \mathcal{H}_{\boldsymbol{k}}$ while preserving parity symmetry $\mathcal{P}\mathcal{H}_{\boldsymbol{k}}\mathcal{P}^{-1} = \mathcal{H}_{-\boldsymbol{k}}$ and time-reversal symmetry $\mathcal{T}\mathcal{H}_{\boldsymbol{k}}\mathcal{T}^{-1} = \mathcal{H}_{-\boldsymbol{k}}$ individually in which we have $\mathcal{P} = \gamma_3$ and $\mathcal{T} = \gamma_3\mathcal{K}$ symmetries with $\mathcal{P}^2 = \mathcal{T}^2 = 1$. Spinless spatial symmetries other than $\mathcal{P}$ preserved when $m_z = 0$ are mirror symmetries $M_{x,y}$ and C_4 symmetry, where $M_{x,y}^2 = 1$, $C_4^4 = 1$ and $C_4^2 = \mathcal{P}$, given by

$$\begin{aligned} M_x\mathcal{H}_{(k_x,k_y)}M_x^{-1} &= \mathcal{H}_{(-k_x,k_y)},\ M_x = \sigma_0 \otimes \tau_3,\\ M_y\mathcal{H}_{(k_x,k_y)}M_y^{-1} &= \mathcal{H}_{(k_x,-k_y)},\ M_y = \sigma_3 \otimes \tau_3, \end{aligned} \tag{A2}$$

and

$$C_4\mathcal{H}_{(k_x,k_y)}C_4^{-1} = \mathcal{H}_{(k_y,-k_x)}, \tag{A3}$$

with

$$C_4 = \begin{pmatrix} i\tau_2 & 0 \\ 0 & -i\tau_0 \end{pmatrix}, \tag{A4}$$

where σ_i and τ_i are Pauli matrices and σ_0 is the 2×2 identity matrix. When $m_z \neq 0$ only the C_4 symmetry is broken.

When $m_z = t_0 = 0$, one can check that this Hamiltonian also preserves additional time-reversal symmetry $\mathcal{T}$ (TRS), particle-hole symmetry $\mathcal{C}$ (PHS), and chiral symmetry $\mathcal{S}$ (CS), given by

$$\begin{aligned} \mathcal{T} &= i\sigma_3 \otimes \tau_2\mathcal{K}, \quad \mathcal{T}^2 = -1,\\ \mathcal{C} &= i\sigma_1 \otimes \tau_3\mathcal{K}, \quad \mathcal{C}^2 = +1,\\ \mathcal{S} &= \sigma_2 \otimes \tau_1, \quad \mathcal{S}^2 = +1. \end{aligned} \tag{A5}$$

When $m_z \neq 0$, PHS and CS and TRS with $\mathcal{T}^2 = -1$ are all broken. In this case classification belongs to AI class in 2D with trivial topology. Thus nontrivial topology is considered to be brought by $\mathcal{PT}$ symmetry rather than $\mathcal{T}^2 = +1$ symmetry alone. In Fig. 4 we show a comparison based on open boundary energy spectrum for $m_z \neq 0$ and $m_z = 0$, where the former one doesn't acquire a pair of zero-energy edge states at $k_x = 0$.

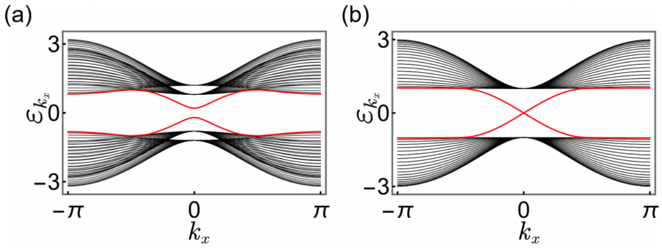

FIG. 4. Energy band spectrum taken in the periodic boundary along x and the open boundary along y in topological nontrivial phase for $\delta_V/t_1 = 2$, $t_2/t_1 = t_3/t_1 = 1$, and $t_0 = 0$ for (a) $m_z/t_1 = 0.4$ and (b) $m_z = 0$. Edge states are labeled in red.

APPENDIX B: DETAILS OF RAMAN AND OPTICAL POTENTIALS

In this Appendix we give details of light fields which generate the proposed potential and the Raman fields given in main text. The light fields are

$$\boldsymbol{E}_x = E_{xz}\boldsymbol{e}_z \cos k_L x + \mathrm{i}E_{xy}\boldsymbol{e}_y \sin k_L x,$$
$$\boldsymbol{E}_y = \sum_{i=1,2} E_{yz}^{(i)}\boldsymbol{e}_z \sin k_L y + E_{yx}\boldsymbol{e}_x \cos k_L y, \tag{B1}$$

where all $E_{\mu\nu}$ are real strength of light fields and $E_{yz}^{(1)} = E_{yz}^{(2)} = E_{yz}$. Setting quantization axis to be parallel to $\hat{z}$, light field $E_{xz,yz}$ drives π transitions, and $E_{xy,yx}$ drives $\sigma_\pm$ transitions by decomposing into the $\hat{e}_\pm$ basis:

$$E_{xy}^{(-)} = -\frac{i}{\sqrt{2}}E_{xy};\ E_{xy}^{(+)} = \frac{i}{\sqrt{2}}E_{xy},$$
$$E_{yx}^{(-)} = \frac{1}{\sqrt{2}}E_{yx};\ E_{yx}^{(+)} = \frac{1}{\sqrt{2}}E_{yx}. \tag{B2}$$

To give a parameter estimation, we make a further calculation in ^{133}Cs atoms as an example. The chosen spin states are $|e_\uparrow\rangle = |F = 4, m_F = 1\rangle$, $|e_\downarrow\rangle = |4, -1\rangle$, $|g_\uparrow\rangle = |3, -1\rangle$, $|g_\downarrow\rangle = |3, 1\rangle$ from ground-state manifold $6S_{1/2}$. The hyperfine splitting is $\delta_F^S \approx 9.20$ GHz in $6S_{1/2}$, $\delta_F^P \approx 1.17$ GHz in $6P_{1/2}$ [96]. An extra magnetic field brings a energy shift estimated by $\delta_B \simeq 100$ MHz, which is much smaller than δ_F, but still much larger than any parameters in an effective Hamiltonian. As mentioned in main text, we have only the D1 transition to be considered, which gives the Raman strength:

$$M_{10} = \frac{1}{16}\sqrt{\frac{5}{3}}\alpha_{D1}^2 E_{xy}E_{yx}\left(\frac{1}{\Delta_1} - \frac{1}{\Delta_2}\right),$$
$$M_{20} = \frac{1}{16}\sqrt{\frac{5}{3}}\alpha_{D1}^2 E_{xz}E_{yz}\left(\frac{1}{\Delta_1} - \frac{1}{\Delta_2}\right), \tag{B3}$$

where $\Delta_2 = \Delta_1 + \delta_F^P$, and $\alpha_{D1} \approx 3.19ea_0$ is the related scalar polarizability with a_0 for the Bohr radius.

A similar direct calculation gives the spin-dependent potential of $|e\rangle$ and $|g\rangle$, given by

$$V_{ex}(x) = \alpha_{D1}E_{xy}^2\left(\frac{13}{96}\frac{1}{\Delta_1 - \Delta_F} + \frac{19}{96}\frac{1}{\Delta_2 - \Delta_F}\right)\sin^2(k_L x)$$
$$+ \alpha_{D1}E_{xz}^2\left(\frac{5}{16}\frac{1}{\Delta_1 - \Delta_F} + \frac{1}{48}\frac{1}{\Delta_2 - \Delta_F}\right)\cos^2(k_L x),$$
$$V_{ey}(y) = \alpha_{D1}E_{yx}^2\left(\frac{13}{96}\frac{1}{\Delta_1} + \frac{19}{96}\frac{1}{\Delta_2}\right)\cos^2(k_L y)$$
$$+ \alpha_{D1}E_{yz}^2\left(\frac{5}{8}\frac{1}{\Delta_1} + \frac{1}{24}\frac{1}{\Delta_2}\right)\sin^2(k_L y),$$
$$V_{gx}(x) = \alpha_{D1}E_{xy}^2\left(\frac{11}{96}\frac{1}{\Delta_1} + \frac{7}{32}\frac{1}{\Delta_2}\right)\sin^2(k_L x)$$
$$+ \alpha_{D1}E_{xz}^2\left(\frac{1}{48}\frac{1}{\Delta_1} + \frac{5}{16}\frac{1}{\Delta_2}\right)\cos^2(k_L x),$$
$$V_{gy}(y) = \alpha_{D1}E_{yx}^2\left(\frac{11}{96}\frac{1}{\Delta_1 + \Delta_F} + \frac{7}{32}\frac{1}{\Delta_2 + \Delta_F}\right)\cos^2(k_L y)$$
$$+ \alpha_{D1}E_{yz}^2\left(\frac{1}{24}\frac{1}{\Delta_1 + \Delta_F} + \frac{5}{8}\frac{1}{\Delta_2 + \Delta_F}\right)\sin^2(k_L y), \tag{B4}$$

where the subscript indicates sublevel and direction. By discarding constants in Eq. (B4) and forcing $\boldsymbol{r} = (0, 0)$ at maximum, we reach a lattice potential $V_{\mathrm{latt}}(x, y) = (V_x\mathbf{1} + \delta V_x\gamma_3)\cos^2(k_L x) + (V_y\mathbf{1} + \delta V_y\gamma_3)\cos^2(k_L y)$, which is further discussed in the isotropic case in the main text. Yet Eq. (B4) holds a greater tunability of generated optical potential, such as a staggered spatial distribution of lattice sites for $|e\rangle$ and $|g\rangle$.

APPENDIX C: FULL-BAND CALCULATIONS

Here we introduce the derivation of results based on continuous Hamiltonian $\hat{H}$. We expand spatial periodic optical potential in the following way:

$$V_e(x, y) = V_{0e} + \tfrac{1}{4}V_{0e}(e^{\mathrm{i}2k_L x} + e^{-\mathrm{i}2k_L x} + e^{\mathrm{i}2k_L y} + e^{-\mathrm{i}2k_L y}),$$
$$V_g(x, y) = V_{0g} + \tfrac{1}{4}V_{0g}(e^{\mathrm{i}2k_L x} + e^{-\mathrm{i}2k_L x} + e^{\mathrm{i}2k_L y} + e^{-\mathrm{i}2k_L y}), \tag{C1}$$

where we set $V_x = V_y = V_0$, $\delta V_x = \delta V_y = \delta_V$, and denote $V_{0e} = V_0 + \delta_V$ and $V_{0g} = V_0 - \delta_V$. The Raman potential is also expressed by

$$\mathcal{M}_1(x, y) = \frac{1}{4\mathrm{i}}M_{10}(e^{\mathrm{i}k_L x} - e^{-\mathrm{i}k_L x})(e^{\mathrm{i}k_L y} + e^{-\mathrm{i}k_L y}),$$
$$\mathcal{M}_2(x, y) = \frac{1}{4\mathrm{i}}M_{20}(e^{\mathrm{i}k_L x} + e^{-\mathrm{i}k_L x})(e^{\mathrm{i}k_L y} - e^{-\mathrm{i}k_L y}), \tag{C2}$$

in which the Raman potentials possess half of period of the optical potential. In a limited area $S = L^2$ with side length L, an orthonormal set of wave functions with quasimomentum $\boldsymbol{k} = (k_x, k_y)$ is $\{\psi_e^{m,n}(\boldsymbol{k})\,|e_\uparrow\rangle, \psi_e^{m,n}(\boldsymbol{k})\,|e_\downarrow\rangle, \psi_g^{m,n}(\boldsymbol{k})\,|g_\uparrow\rangle, \psi_g^{m,n}(\boldsymbol{k})\,|g_\downarrow\rangle\}$ with

$$\psi_e^{m,n}(\boldsymbol{k}) = \frac{1}{L}e^{\mathrm{i}(2mk_L + k_x)x}e^{\mathrm{i}(2nk_L + k_y)y},$$
$$\psi_g^{m,n}(\boldsymbol{k}) = \frac{1}{L}e^{\mathrm{i}(2mk_L + k_L + k_x)x}e^{\mathrm{i}(2nk_L + k_L + k_y)y}, \tag{C3}$$

where the phase difference between $\psi_e^{m,n}$ and $\psi_g^{m,n}$ is brought by Raman processes along the $\pm\hat{e}_x \pm \hat{e}_y$ direction. Under a finite cutoff order $N_{\max}$, such that $|m|, |n| \leqslant N_{\max}$, the Hamiltonian $\hat{H}$ has its matrix representation on this basis, and

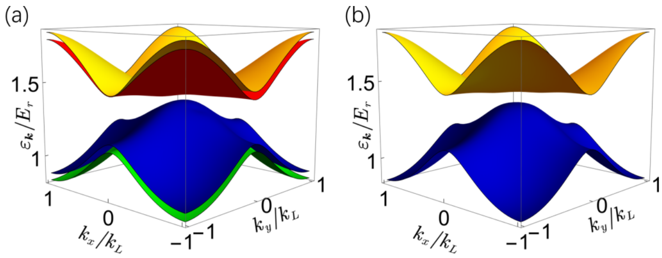

FIG. 5. Band structures for four lowest bands taking part in effective TB model with (a) $m_z = 0.05E_r$ and (b) $m_z = 0$. Other parameters are $V_0 = 3E_r$, $\delta_V = 0.3E_r$, $M_{10} = M_{20} = E_r$. The maximum order $N_{\max} = 5$.

the related eigenproblem reads

$$H\,|\Psi_{\boldsymbol{k}}^l\rangle = \varepsilon_{\boldsymbol{k}}^l\,|\Psi_{\boldsymbol{k}}^l\rangle, \tag{C4}$$

where the eigenfunction of band index l is then given by

$$\begin{aligned}|\Psi_{\boldsymbol{k}}^l\rangle = \sum_{m,n,s=\uparrow,\downarrow} & a_{m,n,s}^l(\boldsymbol{k})\psi_e^{m,n}(\boldsymbol{k})\,|e_s\rangle \\ & + b_{m,n,s}^l(\boldsymbol{k})\psi_g^{m,n}(\boldsymbol{k})\,|g_s\rangle,\end{aligned} \tag{C5}$$

with energy eigenvalue $\varepsilon_{\boldsymbol{k}}^l$. Here we show the complete s-band structure in Fig. 5, with four lowest eigenvalues, which is only partially given in main text. As for primarily giving the topological phase diagram from observables related to $|\Psi_{\boldsymbol{k}}^l\rangle$, we consider the simple case where $m_z = 0$. It's noticed that the Bloch Hamiltonian $\mathcal{H}_{\boldsymbol{k}}$ commutes with g_{02}, which allows us to divide the Hamiltonian into two Chern sections:

$$\mathcal{H}_{\boldsymbol{k}} = \mathcal{H}_c^+ \otimes \sigma_2^+ + \mathcal{H}_c^- \otimes \sigma_2^-, \tag{C6}$$

where $\sigma_2^\pm = |\pm\rangle\langle\pm|$ with $\sigma_2|\pm\rangle = \pm|\pm\rangle$ is a two projected subspace formed by eigenstates of σ_2. Given the original $\mathcal{H}_{\boldsymbol{k}} = \sum_{i=1,2,3} d_i\gamma_i$, the $\mathcal{H}_c^\pm = \sum_i d_i^\pm\sigma_i$ with $\vec{d}_\pm = (d_1, \pm d_2, d_3)$, with preserved parity symmetry $\sigma_3\mathcal{H}_c^\pm(\boldsymbol{k})\sigma_3 = \mathcal{H}_c^\pm(-\boldsymbol{k})$ and identical topological phase characterized by Chern number. Thus second SW class of $\mathcal{H}_{\boldsymbol{k}}$ in this special case is mapped into the Chern number in $\mathcal{H}_c$. We thus apply the minimal measurement for realized quantum anomalous Hall models, taking the criterion based on $\xi = \mathrm{sgn}(\langle\gamma_3\rangle)$ at parity-symmetric points $\Gamma = (0,0)$, $X = (\pi, 0)$, $Y = (0, \pi)$, $M = (\pi, \pi)$ [97],

$$\nu = -\frac{\Theta}{2}\sum_i \xi_i, \tag{C7}$$

where $(-1)^\Theta = \prod_i \xi_i$. For the full-band calculation this can be settled from derived $|\Psi_{\boldsymbol{k}}^l\rangle$:

$$\langle\gamma_3(\boldsymbol{k})\rangle_l = \langle\Psi_{\boldsymbol{k}}^l|\gamma_3|\Psi_{\boldsymbol{k}}^l\rangle, \tag{C8}$$

which is the spin polarization along γ_3 for l in four s bands in zero temperature.

APPENDIX D: CALCULATION OF O_2 LINKS

In main text we have shown the numerical results of extracting real Berry curvature under PBCs and $m_z = 0$. For other conditions, we can still begin with a many-body ground state,

$$|G\rangle = \prod_{i=1}^{\mathcal{N}} a_i^\dagger\,|0\rangle, \tag{D1}$$

where we directly denote creation operators of eigenmodes $|\psi_i\rangle \equiv a_i^\dagger|0\rangle$ in the order of eigenenergies $\varepsilon_i = \langle\psi_i|H_s|\psi_i\rangle$ from the lowest one, and $\mathcal{N} = 2\mathcal{L}^2$ is the number of particles maintaining half-filling with site number $\mathcal{L}$ along one side in the square lattice. Each eigenmode can be formally expanded by a complete basis $|\psi_i\rangle \equiv a_i^\dagger|0\rangle = \sum_{\boldsymbol{r},\alpha}[\psi_i]^{\boldsymbol{r},\alpha}c_{\boldsymbol{r},\alpha}^\dagger|0\rangle$ in which $[\psi_i]^{\boldsymbol{r},\alpha}$ are coefficients related to site at $\boldsymbol{r}$ and spin $\alpha = e_{\uparrow,\downarrow}, g_{\uparrow,\downarrow}$.

To extract all discretized real Berry curvature, all of the following distribution related to quasimomentum is essential for each condition:

$$N_{\alpha\beta}(\boldsymbol{k}) = \langle G|\,c_{\boldsymbol{k},\alpha}^\dagger c_{\boldsymbol{k},\beta}\,|G\rangle, \tag{D2}$$

which assumed to be achievable through tomography by extra pulses and TOF measurements in experiments. In our calculation, this is derived from Fourier transform from site representation, given by

$$\begin{aligned}N_{\alpha\beta}(\boldsymbol{k}) &= \langle G|\,c_{\boldsymbol{k},\alpha}^\dagger c_{\boldsymbol{k},\beta}\,|G\rangle \\ &= \langle G|\,\frac{1}{\mathcal{L}}\sum_{\boldsymbol{r}} e^{i\boldsymbol{k}\cdot\boldsymbol{r}}c_{\boldsymbol{r},\alpha}^\dagger\,\frac{1}{\mathcal{L}}\sum_{\boldsymbol{r}'} e^{-i\boldsymbol{k}\cdot\boldsymbol{r}'}c_{\boldsymbol{r}',\beta}\,|G\rangle \\ &= \frac{1}{\mathcal{L}^2}\sum_{\boldsymbol{r},\boldsymbol{r}'}\langle G|\,c_{\boldsymbol{r},\alpha}^\dagger c_{\boldsymbol{r}',\beta}\,|G\rangle\, e^{i\boldsymbol{k}\cdot(\boldsymbol{r}-\boldsymbol{r}')} \\ &= \frac{1}{\mathcal{L}^2}\sum_{\boldsymbol{r},\boldsymbol{r}',i}[\psi_i^*]^{\boldsymbol{r},\alpha}[\psi_i]^{\boldsymbol{r}',\beta}e^{i\boldsymbol{k}\cdot(\boldsymbol{r}-\boldsymbol{r}')},\end{aligned} \tag{D3}$$

where $[\psi_i^*]^{\boldsymbol{r},\alpha}$ denotes complex conjugate of this coefficient. In an ideal case, $n(\boldsymbol{k})$ is reduced to projector $P_{\boldsymbol{k}} = \sum_\pm |u_{\boldsymbol{k}}^{1\pm}\rangle\langle u_{\boldsymbol{k}}^{1\pm}|$ for occupied bands.

To fix the orientation that might be violated in this numerical process, we have two different ways. As in the main text, we solve Bloch functions explicitly from the northern gauge of stereographic representation, parameterized by

$$\begin{aligned}|u_{\boldsymbol{k}}^{1+}\rangle &= \frac{1}{\sqrt{x_{\boldsymbol{k}}^2 + y_{\boldsymbol{k}}^2 + 1}}(x_{\boldsymbol{k}}, y_{\boldsymbol{k}}, -1, 0), \\ |u_{\boldsymbol{k}}^{1-}\rangle &= \frac{1}{\sqrt{x_{\boldsymbol{k}}^2 + y_{\boldsymbol{k}}^2 + 1}}(-y_{\boldsymbol{k}}, x_{\boldsymbol{k}}, 0, -1),\end{aligned} \tag{D4}$$

in which two pulses are adequate to give full tomography of occupied Bloch states. We take Raman pulse $T_1 = e^{i\frac{\pi}{4}\sigma_2}(T_2 = e^{i\frac{\pi}{4}\gamma_4})$ which turns Bloch components $[u_{\mathbf{k}}^{1\pm}]^1$ into $\frac{1}{\sqrt{2}}([u_{\mathbf{k}}^{1\pm}]^1 + [u_{\mathbf{k}}^{1\pm}]^3)([u_{\mathbf{k}}^{1\pm}]^1$ to $\frac{1}{\sqrt{2}}([u_{\mathbf{k}}^{1\pm}]^1 + [u_{\mathbf{k}}^{1\pm}]^4))$. Parameters $x_{\boldsymbol{k}}$ and $y_{\boldsymbol{k}}$ can be solved from relations $n_{e\uparrow}(\boldsymbol{k}) = \frac{x_{\boldsymbol{k}}^2+y_{\boldsymbol{k}}^2}{\sqrt{1+x_{\boldsymbol{k}}^2+y_{\boldsymbol{k}}^2}}$, $n_{e\uparrow}^{(1)}(\boldsymbol{k}) = \frac{(x_{\boldsymbol{k}}-1)^2+y_{\boldsymbol{k}}^2}{2\sqrt{1+x_{\boldsymbol{k}}^2+y_{\boldsymbol{k}}^2}}$ and $n_{e\uparrow}^{(2)}(\boldsymbol{k}) = \frac{(-y_{\boldsymbol{k}}-1)^2+x_{\boldsymbol{k}}^2}{2\sqrt{1+x_{\boldsymbol{k}}^2+y_{\boldsymbol{k}}^2}}$. It's obvious that the choice of pulses is not unique, and even may be not the simplest. For more general cases, i.e., conditions listed in Table I, the explicit form (D4) is not valid, yet we legitimately assume all elements $N_{\alpha\beta}(\boldsymbol{k})$ can still be obtained through a finite number of Raman pulses. Then the parallel transport

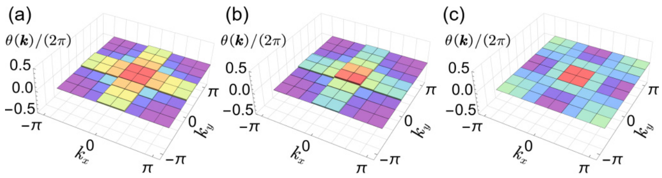

FIG. 6. Discretized Berry curvature with parallel gauge. (a) $\nu = 1$, with $t_2/t_1 = t_3/t_1 = 1$, $\delta_V/t_1 = 2$, and $m_z = 0$, under PBCs, which is the same condition as in the main text. (b) $\nu = 0.999$, with $t_2/t_1 = t_3/t_1 = 1$, $\delta_V/t_1 = 2$, and $m_z/t_1 = 0.4$, under OBCs. (c) $\nu = 0$, with $t_2/t_1 = t_3/t_1 = 1$, $\delta_V/t_1 = 8$, and $m_z/t_1 = 0.4$, under OBCs.

gauge is applied to fix the orientation. This gauge is also called the cylinder gauge, in which wave functions are smooth inside the whole FBZ but the periodicity is kept for only one direction and broken for the other due to Wannier obstruction. We show some related results in Fig. 6. In contrast to the figure in the main text which is derived from exhibiting accumulation of local real Berry curvature near the south pole, the distribution calculated by the parallel transport gauge varies mildly.

APPENDIX E: BULK-SURFACE DUALITY FROM DEFORMATION OF $\mathcal{PT}$-SYMMETRIC BLOCH HAMILTONIAN

In this section we discuss further extracting nontrivial topology from the BISs. To see this, for simplicity we take a general spherical representation of the normalized Hamiltonian $H_{\boldsymbol{k}} = \vec{d} \cdot \vec{\gamma}$ such that where $\vec{d} = (\sin\theta_{\boldsymbol{k}}, \cos\theta_{\boldsymbol{k}} \sin\varphi_{\boldsymbol{k}}, \cos\theta_{\boldsymbol{k}} \cos\varphi_{\boldsymbol{k}})$ is related with the coordinate of a point on a sphere. A gauge-invariant description of ν for $H_{\boldsymbol{k}} = \vec{d} \cdot \vec{\gamma}$ can be given by

$$\begin{aligned} \nu &= \int_{T^2} -\frac{\mathrm{i}}{32\pi} \mathrm{Tr}[\tau_2 H_{\boldsymbol{k}} (\mathrm{d}H_{\boldsymbol{k}})^2] \\ &= \frac{1}{8\pi} \int_{T^2} d^2\boldsymbol{k} \epsilon_{ijk} d_i (\nabla_{\boldsymbol{k}} d_j \times \nabla_{\boldsymbol{k}} d_k)_z, \end{aligned} \tag{E1}$$

where we use the relation $\mathrm{Tr}[\tau_2 \gamma_i \gamma_j \gamma_k] = 4\mathrm{i}\epsilon_{ijk}$. The topology for $H_{\boldsymbol{k}}$ should be equivalent with another deformed Hamiltonian of $h(\boldsymbol{k}) = \vec{d}' \cdot \vec{\gamma}$ where $\vec{d}' = (\sin\Theta_{\boldsymbol{k}}, \cos\Theta_{\boldsymbol{k}} \sin\varphi_{\boldsymbol{k}}, \cos\Theta_{\boldsymbol{k}} \cos\varphi_{\boldsymbol{k}})$ and $\Theta_{\boldsymbol{k}}$ could be any monotomic function since both the energy gap and $\mathcal{PT}$-symmetry are preserved [84]. Substituting into Eq. (E1), the topological invariant is written by $\nu = 1/(4\pi) \oint d^2\boldsymbol{k} \cos\Theta_{\boldsymbol{k}} [(\nabla_{\boldsymbol{k}}\Theta_{\boldsymbol{k}}) \times (\nabla_{\boldsymbol{k}}\varphi_{\boldsymbol{k}})]_z$. Under an extreme choice of $\Theta_{\boldsymbol{k}}$ such that

$$\cos\Theta_{\boldsymbol{k}} = \begin{cases} 1, & \boldsymbol{k} \in \text{BISs} \\ 0, & \text{otherwise} \end{cases} \tag{E2}$$

and $\nabla\Theta_{\boldsymbol{k}} = \delta(\boldsymbol{k} - \boldsymbol{k}_{\text{BISs}})$, Eq. (E1) is then reduced into a line integral on closed 1D 1-BISs with an exact winding number form $\nu = 1/(2\pi) \oint_{\text{BIS}} d\boldsymbol{k} \nabla_{\boldsymbol{k}} \varphi_{\boldsymbol{k}}$ defined on the 1-BISs for γ_1. Since we don't acquire any explicit form of Hamiltonian in this derivation, the choice of the reduced component γ_1 is indeed arbitrary. This can be iteratively done to reach higher-order BISs, as long as the deformation is valid.

[1] D.-W. Zhang, Y.-Q. Zhu, Y. X. Zhao, H. Yan, and S.-L. Zhu, Topological quantum matter with cold atoms, Adv. Phys. **67**, 253 (2018).
[2] N. Goldman, G. Juzeliūnas, P. Öhberg, and I. B. Spielman, Light-induced gauge fields for ultracold atoms, Rep. Prog. Phys. **77**, 126401 (2014).
[3] F. Mei, S.-L. Zhu, Z.-M. Zhang, C. H. Oh, and N. Goldman, Simulating Z_2 topological insulators with cold atoms in a one-dimensional optical lattice, Phys. Rev. A **85**, 013638 (2012).
[4] D.-W. Zhang, Y. X. Zhao, R.-B. Liu, Z.-Y. Xue, S.-L. Zhu, and Z. D. Wang, Quantum simulation of exotic $\mathcal{PT}$-invariant topological nodal loop bands with ultracold atoms in an optical lattice, Phys. Rev. A **93**, 043617 (2016).
[5] M. Z. Hasan and C. L. Kane, Colloquium: Topological insulators, Rev. Mod. Phys. **82**, 3045 (2010).
[6] X.-L. Qi and S.-C. Zhang, Topological insulators and superconductors, Rev. Mod. Phys. **83**, 1057 (2011).
[7] C.-K. Chiu, J. C. Y. Teo, A. P. Schnyder, and S. Ryu, Classification of topological quantum matter with symmetries, Rev. Mod. Phys. **88**, 035005 (2016).
[8] X.-G. Wen, Colloquium: Zoo of quantum-topological phases of matter, Rev. Mod. Phys. **89**, 041004 (2017).
[9] A. P. Schnyder, S. Ryu, A. Furusaki, and A. W. W. Ludwig, Classification of topological insulators and superconductors in three spatial dimensions, Phys. Rev. B **78**, 195125 (2008).
[10] A. Kitaev, Periodic table for topological insulators and superconductors, AIP Conf. Proc. **1134**, 22 (2009).
[11] S. Ryu, A. P. Schnyder, A. Furusaki, and A. W. W. Ludwig, Topological insulators and superconductors: Tenfold way and dimensional hierarchy, New J. Phys. **12**, 065010 (2010).
[12] H. C. Po, A. Vishwanath, and H. Watanabe, Symmetry-based indicators of band topology in the 230 space groups, Nat. Commun. **8**, 50 (2017).
[13] J. Kruthoff, J. de Boer, J. van Wezel, C. L. Kane, and R.-J. Slager, Topological classification of crystalline insulators through band structure combinatorics, Phys. Rev. X **7**, 041069 (2017).
[14] H. C. Po, H. Watanabe, and A. Vishwanath, Fragile topology and Wannier obstructions, Phys. Rev. Lett. **121**, 126402 (2018).
[15] B. Bradlyn, Z. Wang, J. Cano, and B. A. Bernevig, Disconnected elementary band representations, fragile topology, and Wilson loops as topological indices: An example on the triangular lattice, Phys. Rev. B **99**, 045140 (2019).
[16] S. H. Kooi, G. van Miert, and C. Ortix, Classification of crystalline insulators without symmetry indicators: Atomic and fragile topological phases in twofold rotation symmetric systems, Phys. Rev. B **100**, 115160 (2019).
[17] A. Bouhon, A. M. Black-Schaffer, and R.-J. Slager, Wilson loop approach to fragile topology of split elementary band representations and topological crystalline insulators with time-reversal symmetry, Phys. Rev. B **100**, 195135 (2019).
[18] A. Bouhon, T. Bzdusek, and R.-J. Slager, Geometric approach to fragile topology beyond symmetry indicators, Phys. Rev. B **102**, 115135 (2020).

[19] W. A. Benalcazar, B. A. Bernevig, and T. L. Hughes, Quantized electric multipole insulators, Science **357**, 61 (2017).

[20] W. A. Benalcazar, B. A. Bernevig, and T. L. Hughes, Electric multipole moments, topological multipole moment pumping, and chiral hinge states in crystalline insulators, Phys. Rev. B **96**, 245115 (2017).

[21] F. Schindler, A. M. Cook, M. G. Vergniory, Z. Wang, S. S. P. Parkin, B. A. Bernevig, and T. Neupert, Higher-order topological insulators, Sci. Adv. **4**, eaat0346 (2018).

[22] B. Xie, H.-X. Wang, X. Zhang, P. Zhan, J.-H. Jiang, M. Lu, and Y. Chen, Higher-order band topology, Nat. Rev. Phys. **3**, 520 (2021).

[23] C. Fang, Y. Chen, H.-Y. Kee, and L. Fu, Topological nodal line semimetals with and without spin-orbital coupling, Phys. Rev. B **92**, 081201(R) (2015).

[24] Y. X. Zhao and Y. Lu, $\mathcal{PT}$-symmetric real Dirac fermions and semimetals, Phys. Rev. Lett. **118**, 056401 (2017).

[25] K. Wang, J. X. Dai, L. B. Shao, S. A. Yang, and Y. X. Zhao, Boundary criticality of $\mathcal{PT}$-invariant topology and second-order nodal-line semimetals, Phys. Rev. Lett. **125**, 126403 (2020).

[26] A. Bouhon, Q.S. Wu, R.-J. Slager, H. Weng, O. V. Yazyev, and T. Bzdusek, Non-Abelian reciprocal braiding of Weyl points and its manifestation in ZrTe, Nat. Phys. **16**, 1137 (2020).

[27] F. Nur Unal, A. Bouhon, and R.-J. Slager, Topological Euler class as a dynamical observable in optical lattices, Phys. Rev. Lett. **125**, 053601 (2020).

[28] J. Ahn, D. Kim, Y. Kim, and B.-J. Yang, Band topology and linking structure of nodal line semimetals with Z_2 monopole charges, Phys. Rev. Lett. **121**, 106403 (2018).

[29] J. Ahn, S. Park, and B.-J. Yang, Failure of Nielsen-Ninomiya theorem and fragile topology in two-dimensional systems with space-time inversion symmetry: Application to twisted bilayer graphene at magic angle, Phys. Rev. X **9**, 021013 (2019).

[30] Q. Wu, A. A. Soluyanov, and T. Bzdusek, Non-Abelian band topology in noninteracting metals, Science **365**, 1273 (2019).

[31] M. Ezawa, Topological Euler insulators and their electric circuit realization, Phys. Rev. B **103**, 205303 (2021).

[32] R. Takahashi and T. Ozawa, Bulk-edge correspondence of Stiefel-Whitney and Euler insulators through the entanglement spectrum and cutting procedure, Phys. Rev. B **108**, 075129 (2023).

[33] Y. X. Zhao, Andreas P. Schnyder, and Z. D. Wang, Unified theory of PT and CP invariant topological metals and nodal superconductors, Phys. Rev. Lett. **116**, 156402 (2016).

[34] H. Lim, S. Kim, and B.-J. Yang, Real Hopf insulator, arXiv:2303.13078.

[35] A. Bouhon, Y.-Q. Zhu, R.-J. Slager, and G. Palumbo, Second Euler number in four dimensional synthetic matter, arXiv:2301.08827.

[36] W. Zhao, Y.-B. Yang, Y. Jiang, Z. Mao, W. Guo, L. Qiu, G. Wang, L. Yao, L. He, Z. Zhou *et al.*, Quantum simulation for topological Euler insulators, Commun. Phys. **5**, 223 (2022).

[37] S.-L. Zhu, B. Wang, and L.-M. Duan, Simulation and detection of Dirac fermions with cold atoms in an optical lattice, Phys. Rev. Lett. **98**, 260402 (2007).

[38] L. B. Shao, S.-L. Zhu, L. Sheng, D. Y. Xing, and Z. D. Wang, Realizing and detecting the quantum Hall effect without Landau levels by using ultracold atoms, Phys. Rev. Lett. **101**, 246810 (2008).

[39] L. Tarruell, D. Greif, T. Uehlinger, G. Jotzu, and T. Esslinger, Creating, moving and merging Dirac points with a Fermi gas in a tunable honeycomb lattice, Nature (London) **483**, 302 (2012).

[40] D.-W. Zhang, L.-Z. Tang, L.-J. Lang, H. Yan, and S.-L. Zhu, Non-Hermitian topological Anderson insulators, Sci. China Phys. Mech. Astron. **63**, 267062 (2020).

[41] S.-L. Zhu, Z.-D. Wang, Y.-H. Chan, and L.-M. Duan, Topological Bose-Mott insulators in a one-dimensional optical superlattice, Phys. Rev. Lett. **110**, 075303 (2013).

[42] D.-W. Zhang, Y.-L. Chen, G.-Q. Zhang, L.-J. Lang, Z. Li, and S.-L. Zhu, Skin superfluid, topological Mott insulators, and asymmetric dynamics in an interacting non-Hermitian Aubry-André-Harper model, Phys. Rev. B **101**, 235150 (2020).

[43] G. Jotzu, M. Messer, R. Desbuquois, M. Lebrat, T. Uehlinger, D. Greif, and T. Esslinger, Experimental realization of the topological Haldane model with ultracold fermions, Nature (London) **515**, 237 (2014).

[44] B. Song, C. He, S. Niu, L. Zhang, Z. Ren, X.-J. Liu, and G.-B. Jo, Observation of nodal-line semimetal with ultracold fermions in an optical lattice, Nat. Phys. **15**, 911 (2019).

[45] J. Minguzzi, Z. Zhu, K. Sandholzer, A.-S. Walter, K. Viebahn, and T. Esslinger, Topological pumping in a Floquet-Bloch band, Phys. Rev. Lett. **129**, 053201 (2022).

[46] J. Dalibard, F. Gerbier, G. Juzeliūnas, and P. Öhberg, Colloquium: Artificial gauge potentials for neutral atoms, Rev. Mod. Phys. **83**, 1523 (2011).

[47] S.-L. Zhu, H. Fu, C.-J. Wu, S.-C. Zhang, and L.-M. Duan, Spin Hall effects for cold atoms in a light-induced gauge potential, Phys. Rev. Lett. **97**, 240401 (2006).

[48] M. C. Beeler, R. A. Williams, K. Jiménez-García, L. J. LeBlanc, A. R. Perry, and I. B. Spielman, The spin Hall effect in a quantum gas, Nature (London) **498**, 201 (2013).

[49] Y.-J. Lin, R. L. Compton, A. R. Perry, W. D. Phillips, J. V. Porto, and I. B. Spielman, Bose-Einstein condensate in a uniform light-induced vector potential, Phys. Rev. Lett. **102**, 130401 (2009).

[50] J. Ruseckas, G. Juzeliūnas, P. Öhberg, and M. Fleischhauer, Non-Abelian gauge potentials for ultracold atoms with degenerate dark states, Phys. Rev. Lett. **95**, 010404 (2005).

[51] D. Jaksch and P. Zoller, Creation of effective magnetic fields in optical lattices: The Hofstadter butterfly for cold neutral atoms, New J. Phys. **5**, 56 (2003).

[52] N. Goldman, A. Kubasiak, A. Bermudez, P. Gaspard, M. Lewenstein, and M. A. Martin-Delgado, Non-Abelian optical lattices: Anomalous quantum Hall effect and Dirac fermions, Phys. Rev. Lett. **103**, 035301 (2009).

[53] F. Gorg, K. Sandholzer, J. Minguzzi, R. Desbuquois, M. Messer, and T. Esslinger, Realization of density-dependent Peierls phases to engineer quantized gauge fields coupled to ultracold matter, Nat. Phys. **15**, 1161 (2019).

[54] Y.-J. Lin, K. Jiménez-García, and I. Spielman, Spin–orbit-coupled Bose–Einstein condensates, Nature (London) **471**, 83 (2011).

[55] V. Galitski and I. Spielman, Spin–orbit coupling in quantum gases, Nature (London) **494**, 49 (2013).

[56] Z.-C. Xu, Z. Zhou, E. Cheng, L.-J. Lang, and S.-L. Zhu, Gain/loss effects on spin-orbit coupled ultracold atoms in two-dimensional optical lattices, Sci. China Phys. Mech. Astron. **65**, 283011 (2022).

[57] X.-F. Zhou, G.-C. Guo, W. Zhang, and W. Yi, Exotic pairing states in a Fermi gas with three-dimensional spin-orbit coupling, Phys. Rev. A **87**, 063606 (2013).
[58] X. Cui and W. Yi, Universal Borromean binding in spin-orbit-coupled ultracold Fermi gases, Phys. Rev. X **4**, 031026 (2014).
[59] B.-Z. Wang, Y.-H. Lu, W. Sun, S. Chen, Y. Deng, and X.-J. Liu, Dirac-, Rashba-, and Weyl-type spin-orbit couplings: Toward experimental realization in ultracold atoms, Phys. Rev. A **97**, 011605(R) (2018).
[60] J.-H. Zhang, B.-B. Wang, F. Mei, J. Ma, L. Xiao, and S. Jia, Topological optical Raman superlattices, Phys. Rev. A **105**, 033310 (2022).
[61] G. Liu, S.-L. Zhu, S. Jiang, F. Sun, and W. M. Liu, Simulating and detecting the quantum spin Hall effect in the kagome optical lattice, Phys. Rev. A **82**, 053605 (2010).
[62] D.-W. Zhang, Z.-Y. Xue, H. Yan, Z. D. Wang, and Shi-Liang Zhu, Macroscopic Klein tunneling in spin-orbit-coupled Bose-Einstein condensates, Phys. Rev. A **85**, 013628 (2012).
[63] S. L. Zhu, L. B. Shao, Z. D. Wang, and L. M. Duan, Probing non-Abelian statistics of Majorana fermions in ultracold atomic superfluid, Phys. Rev. Lett. **106**, 100404 (2011).
[64] X.-C. Zhou, T.-H. Yang, Z.-Y. Wang, and X.-J. Liu, Non-Abelian dynamical gauge field and topological superfluids in optical Raman lattice, arXiv:2309.12923.
[65] L. Huang, Z. Meng, P. Wang, P. Peng, S.-L. Zhang, L. Chen, D. Li, Q. Zhou, and J. Zhang, Experimental realization of two-dimensional synthetic spin-orbit coupling in ultracold Fermi gases, Nat. Phys. **12**, 540 (2016).
[66] J.-Z. Li, C.-J. Zou, Y.-X. Du, Q.-X. Lv, W. Huang, Z.-T. Liang, D.-W. Zhang, H. Yan, S. Zhang, and S.-L. Zhu, Synthetic topological vacua of Yang-Mills fields in Bose-Einstein condensates, Phys. Rev. Lett. **129**, 220402 (2022).
[67] Z. Wu *et al.*, Realization of two-dimensional spin-orbit coupling for Bose-Einstein condensates, Science **354**, 83 (2016).
[68] Z.-Y. Wang *et al.*, Realization of an ideal Weyl semimetal band in a quantum gas with 3D spin-orbit coupling, Science **372**, 271 (2021).
[69] Q.-X. Lv *et al.*, Measurement of non-Abelian gauge fields using multiloop amplification, Phys. Rev. A **108**, 023316 (2023).
[70] Q.-X. Lv *et al.*, Measurement of spin Chern numbers in quantum simulated topological insulators, Phys. Rev. Lett. **127**, 136802 (2021).
[71] D. A. Abanin, T. Kitagawa, I. Bloch, and E. Demler, Interferometric approach to measuring band topology in 2D optical lattices, Phys. Rev. Lett. **110**, 165304 (2013).
[72] M. Atala, M. Aidelsburger, J. T. Barreiro, D. Abanin, T. Kitagawa, E. Demler, and I. Bloch, Direct measurement of the Zak phase in topological Bloch bands, Nat. Phys. **9**, 795 (2013).
[73] F. Grusdt, D. Abanin, and E. Demler, Measuring $\mathbb{Z}_2$ topological invariants in optical lattices using interferometry, Phys. Rev. A **89**, 043621 (2014).
[74] M. Aidelsburger, M. Lohse, C. Schweizer, M. Atala, J. T. Barreiro, S. Nascimbéne, N. R. Cooper, I. Bloch, and N. Goldman, Measuring the Chern number of Hofstadter bands with ultracold bosonic atoms, Nat. Phys. **11**, 162 (2015).
[75] A. Dauphin and N. Goldman, Extracting the Chern number from the dynamics of a Fermi gas: Implementing a quantum Hall bar for cold atoms, Phys. Rev. Lett. **111**, 135302 (2013).
[76] M. Tarnowski, F. NurÍnal, N. Fläschner, B. S. Rem, A. Eckardt, K. Sengstock, and C. Weitenberg, Measuring topology from dynamics by obtaining the Chern number from a linking number, Nat. Commun. **10**, 1728 (2019).
[77] M. Di Liberto, N. Goldman, and G. Palumbo, Non-Abelian Bloch oscillations in higher-order topological insulators, Nat. Commun. **11**, 5942 (2020).
[78] E. Alba, X. Fernandez-Gonzalvo, J. Mur-Petit, J. K. Pachos, and J. J. Garcia-Ripoll, Seeing topological order in time-of-flight measurements, Phys. Rev. Lett. **107**, 235301 (2011).
[79] P. Hauke, M. Lewenstein, and A. Eckardt, Tomography of band insulators from quench dynamics, Phys. Rev. Lett. **113**, 045303 (2014).
[80] T. Li, L. Duca, M. Reitter, F. Grusdt, E. Demler, M. Endres, M. Schleier-Smith, I. Bloch, and U. Schneider, Bloch state tomography using Wilson lines, Science **352**, 1094 (2016).
[81] R.-B. Liu, D.-L. Deng, D.-W. Zhang, and S.-L. Zhu, Directly probing the Chern number of the Haldane model in optical lattices, J. Opt. Soc. Am. B **32**, 2500 (2015).
[82] N. Fläschner, B. S. Rem, M. Tarnowski, D. Vogel, D.-S. Lühmann, K. Sengstock, and C. Weitenberg, Experimental reconstruction of the Berry curvature in a Floquet Bloch band, Science **352**, 1091 (2016).
[83] C.-R. Yi, J. Yu, H. Yuan, R.-H. Jiao, Y.-M. Yang, X. Jiang, J.-Y. Zhang, S. Chen, and J.-W. Pan, Extracting the quantum geometric tensor of an optical Raman lattice by Bloch-state tomography, Phys. Rev. Res. **5**, L032016 (2023).
[84] L. Zhang, L. Zhang, S. Niu, and X.-J. Liu, Dynamical classification of topological quantum phases, Sci. Bull. **63**, 1385 (2018).
[85] X.-L. Yu, W. Ji, L. Zhang, Y. Wang, J. Wu, and X.-J. Liu, Quantum dynamical characterization and simulation of topological phases with high-order band inversion surfaces, Phys. Rev. X Quantum **2**, 020320 (2021).
[86] J.-Y. Zhang, C.-R. Yi, L. Zhang, R.-H. Jiao, K.-Y. Shi, H. Yuan, W. Zhang, X.-J. Liu, S. Chen, and J.-W. Pan, Tuning anomalous floquet topological bands with ultracold atoms, Phys. Rev. Lett. **130**, 043201 (2023).
[87] A. A. Soluyanov and D. Vanderbilt, Smooth gauge for topological insulators, Phys. Rev. B **85**, 115415 (2012).
[88] L. M. Duan, Detecting correlation functions of ultracold atoms through Fourier sampling of time-of-flight images, Phys. Rev. Lett. **96**, 103201 (2006).
[89] D.-L. Deng, S.-T. Wang, and L.-M. Duan, Direct probe of topological order for cold atoms, Phys. Rev. A **90**, 041601(R) (2014).
[90] C. Monroe, W.C. Campbell, L.-M. Duan, Z.-X. Gong, A.V. Gorshkov, P.W. Hess, R. Islam, K. Kim, N.M. Linke, G. Pagano *et al.*, Programmable quantum simulations of spin systems with trapped ions, Rev. Mod. Phys. **93**, 025001 (2021).
[91] S. L. Zhu, C. Monroe, and L. M. Duan, Trapped ion quantum computation with transverse phonon modes, Phys. Rev. Lett. **97**, 050505 (2006).
[92] F. Mei, Q. Guo, Y.-F. Yu, L. Xiao, S.-L. Zhu, and S. Jia, Digital simulation of topological matter on programmable quantum processors, Phys. Rev. Lett. **125**, 160503 (2020).
[93] I. M. Georgescu, S. Ashhab, and F. Nori, Quantum simulation, Rev. Mod. Phys. **86**, 153 (2014).

[94] X. Tan, D.-W. Zhang, Q. Liu, G. Xue, H.-F. Yu, Y.-Q. Zhu, H. Yan, S.-L. Zhu, and Y. Yu, Topological Maxwell metal bands in a superconducting qutrit, Phys. Rev. Lett. **120**, 130503 (2018).

[95] X. Tan, D.-W. Zhang, Z. Yang, J. Chu, Y.-Q. Zhu, D. Li, X. Yang, S. Song, Z. Han, Z. Li *et al.*, Experimental measurement of the quantum metric tensor and related topological phase transition with a superconducting qubit, Phys. Rev. Lett. **122**, 210401 (2019).

[96] D. A. Steck, Cesium D line data, v.2.3.2, https://steck.us/alkalidata/cesiumnumbers.pdf (Sept. 2023).

[97] X.-J. Liu, K. T. Law, T. K. Ng, and P. A. Lee, Detecting topological phases in cold atoms, Phys. Rev. Lett. **111**, 120402 (2013).